JTTEE5 19:779–786
DOI: 10.1007/s11666-010-9474-3
1059-9630/$19.00 © ASM International

Peer Reviewed

Assessing Coating Reliability Through Pore Architecture Evaluation

S. Paul

(Submitted July 15, 2009; in revised form December 5, 2009)

Plasma-sprayed thermal barrier coatings (TBCs) exhibit many interlamellar pores, voids, and microcracks. These microstructural features are primarily responsible for the low global stiffness and the low thermal conductivity commonly exhibited by such coatings. The pore architecture thus has an important influence on such thermophysical properties. In the present work, the effect of heat treatment (at temperatures up to 1400 °C, for times of up to 20 h) on the pore architecture of detached YSZ top coats with different impurity levels have been characterized by mercury intrusion porosimetry and gas-sorption techniques. Stiffness and thermal conductivity were also monitored to assess the effect of change in pore architecture on properties. While the overall porosity level remained relatively unaffected (at around 10-12%) after the heat treatments concerned, there were substantial changes in the pore size distribution and the (surface-connected) specific surface area. Fine pores (<~50 nm) rapidly disappeared, while the specific surface area dropped dramatically, particularly at high-treatment temperatures (~1400 °C). These changes are thought to be associated with intrasplat microcrack healing, improved intersplat bonding and increased contact area, leading to disappearance of much of the fine porosity. These microstructural changes are reflected in sharply increased stiffness and thermal conductivity. Increase in thermal conductivity and stiffness were found to be more pronounced for coatings with higher impurity content (particularly alumina and silica). Reliability issues surrounding such increase in thermal conductivity and stiffness are discussed along with a brief note on the effect of impurities on TBC life.

Keywords impurities, plasma-sprayed coatings, pore architecture, sintering, stiffness, thermal conductivity

1. Introduction

Ceramic thermal barrier coatings (TBCs) are being increasingly used to protect metallic components of gas turbines exposed to elevated temperatures by exploiting their physical properties—primarily low thermal conductivity and high strain tolerance (Ref 1-4). These physical properties, a consequence of pore architecture resulting from the coating process, are prone to change under service conditions. Such changes could impair the performance of these coatings as TBCs. Understanding the changes in pore architecture and relating it to changes in properties in-service thus forms an important objective.

Typical TBC systems are composed of a YSZ top coat about 100-500 μm in thickness, deposited either by atmospheric plasma spray (APS) or electron beam physical vapor deposition (EB-PVD) onto a metallic bond coat. Plasma-sprayed deposits are composed of splats created by quenching of molten or sometimes semi-molten feedstock particles either on a bare substrate or on a layer of previously deposited particles. This rapid cooling of the splats results in the formation of large number of microcracks. The through-thickness microcracks relax a lot of the quenching stress generated during plasma spraying (Ref 5).

Common features of the microstructure of APS coatings are shown in Fig. 1. Presence of such microstructural features give rise to its low-macroscopic stiffness and thermal conductivity. These microstructural features can be significantly affected by prolonged exposure to high temperature usually experienced by these coatings in service (Ref 6-8). An illustration of how both inter and intrasplat pores can partially heal via sintering at elevated temperature is provided by micrograph in Fig. 2.

There is concern that such sintering-induced changes that occur under service conditions may adversely affect the protective function of the coating. In addition to thermal conductivity, the stiffness of the coating is also important as the strain compliance is governed by it. The stress (σ_c) in the coating during cooling from T_2 to T_1 in service is a linear function of its Young's modulus E_c as given by Eq 1.

$$\sigma_c = -\frac{E_c \int_{T_1}^{T_2} (\alpha_s(T) - \alpha_c(T))dT}{(1-\nu)\left(1 + \frac{E_c h_c}{E_s\left(\frac{h_s+h_c}{2}\right)}\right)} \quad \text{(Eq 1)}$$

Here, E_s is the Young's modulus of the substrate, h_c and h_s are the thicknesses of, respectively, coating (usually thin) and substrate (usually thick); α is the corresponding linear thermal expansion coefficient; ν is the Poisson's ratio, assumed to be 0.3 for coating and substrate.

S. Paul, Department of Materials Science & Metallurgy, University of Cambridge, Cambridge CB2 3QZ, UK and TWI, Cambridge CB21 6AL, UK. Contact e-mail: sp367@cam.ac.uk.

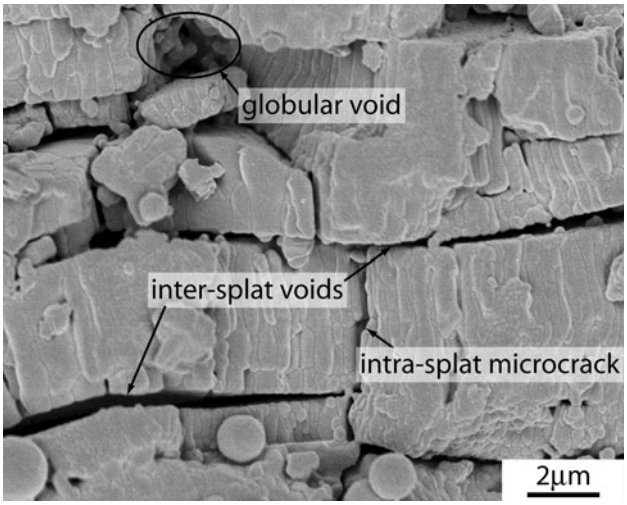

Fig. 1 Typical microstructural features of as-sprayed TBC top coat

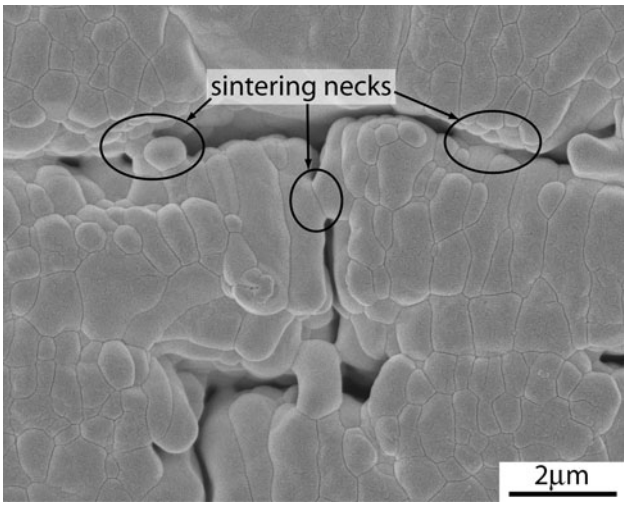

Fig. 2 Micrograph of a top coat heat treated at 1400 °C for 10 h

The stress generated in the top coat during cooling can cause spallation under in-plane compression either by buckling or wedging depending on the oxide/coating interfacial strength. In general, it is likely that the top coat will remain adherent to the substrate until its stored strain energy (G_c) per unit area of the top coat/metal interface at a temperature drop ($\Delta T = T_2 - T_1$) is sufficient to produce decohesion of the interface (Ref 9). This is given by Eq 2:

$$G_c = h_c E_c (1-\nu)\left(\int_{T_1}^{T_2} (\alpha_s(T) - \alpha_c(T))dT\right)^2 \qquad \text{(Eq 2)}$$

The implications of Eq 1 and 2 are shown in Fig. 3 where the effect of different coating and substrate properties are elucidated. The average thermal expansion coefficient of

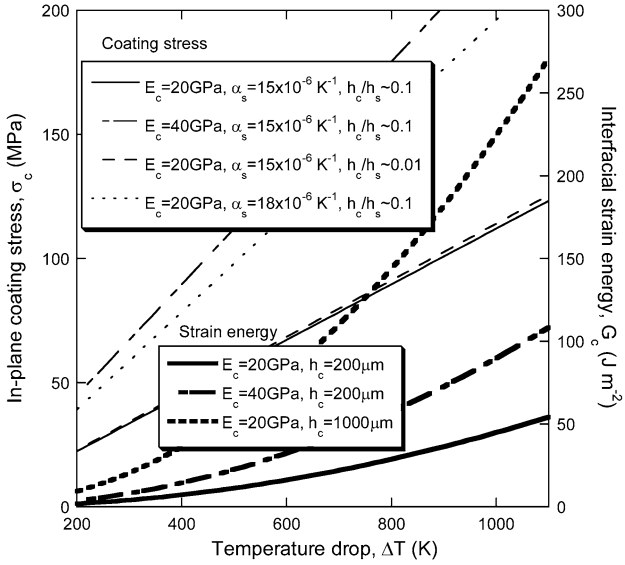

Fig. 3 Effect of materials properties (and temperature drop) on the in-plane coating stress and interfacial strain energy of a YSZ coating on a stiff substrate ($E_s = 200$ GPa). Notations have the same meaning as in Eq 1 and 2

the coating was assumed to be ~11 × 10^{-6} K^{-1} for the calculations. The plot emphasizes the importance of sintering-induced property changes (particularly stiffness) on the life of a TBC system.

Sintering of YSZ TBCs has been the subject of a number of publications (Ref 6-8, 10-16) where researchers applied various methods (often involving fairly complex computational analysis) to understand the processes. Some similar as in this work (Ref 11, 12), some more unique involving more expensive equipment like small-angle neutron scattering (Ref 7, 8) and some using quantitative image analysis (Ref 16). However, in most of these works only one chosen aspect of the sintering process has been explored and the drawbacks in the techniques used for analysis rarely stated. Although, microstructure-property relationships have been studied extensively, very few publications address the effect of impurities such as silica and alumina on the microstructure, and hence properties of plasma-sprayed top coats. The ones that do (Ref 11, 12, 17) only focus either on microstructural or property changes, and none seem to address and correlate the pore architectural changes with properties in service and hence the life of the different top coats. This area of research needs particular attention considering the problems our modern aero-engines face that operate in dust-laden environments. Ingestion of particulates (rich in alumina, silica, etc.) into the gas turbine engine has a harmful effect on the TBCs as they are highly susceptible to degradation by molten CMAS (calcium-magnesium-alumino-silicate) deposits.

Thus, there is need for data to assess the effect of different contaminants (particularly silica and alumina) on the pore architecture which governs the physical properties of the coatings, and ultimately the life of a TBC system.

In the present work, this has been addressed. A number of coatings with different YSZ chemistry has been prepared and carefully controlled. Their microstructure and properties have been studied in details before and after various heat treatments, and conclusions drawn from these data regarding their life in service.

2. Experimental Procedure

2.1 Sample Preparation

2.1.1 Coating Production. Coatings, designated AB1 and AB2, were produced by atmospheric plasma spraying using the conditions listed in Table 1. The compositions of the powders used are given in Table 2. Prior to all tests, the top coat was de-bonded from the mild steel substrate by treating it with hydrochloric acid.

2.1.2 Heat Treatment. The detached top coats were isothermally heat treated in air at 1200 and 1400 °C for different times. A heating rate of ~20 °C min^{-1} was used, while cooling after the heat treatment was carried out by simply removing the sample from the furnace.

2.2 Dimensional, Stiffness, and Thermal Conductivity Changes

2.2.1 Dilatometry. Dimensional change during isothermal heat treatment was monitored using DIL 402C dilatometer (Netzsch, Selb, Germany). Dilatometry was performed on detached top coats, in both in-plane and through-thickness directions.

2.2.2 Stiffness Measurement. Stiffness measurements were made using a purpose-built four-point bending rig. Load was applied via a counter-balanced platen, using small pre-weighed masses and displacements were measured using a scanning laser extensimeter. The elastic behavior was confirmed by checking the linearity and reversibility of the load-deflection plots.

2.2.3 Thermal Conductivity Measurement. Thermal conductivity of the detached top coats was measured using both HotDisk® method (Ref 18) and a simple steady-state bi-substrate technique. The bi-substrate technique is based on establishing a steady-state heat flow through the sample, sandwiched between a pair of metallic blocks with known thermal properties. Full details of the setup can be found elsewhere (Ref 19).

Table 1 Plasma spraying parameters

Chamber pressure	Atmospheric
Stand-off distance, mm	105
Arc current, A	500
Voltage, V	70
Gun speed, mm s^{-1}	55
Gun type	9 MB
Nozzle internal diameter, mm	6
Ar flow rate, l m^{-1}	75
H_2 flow rate, l m^{-1}	20
Scanning step, mm	8

Table 2 Chemical composition of powders (wt.%)

	AB1	AB2
Y_2O_3	7.7	7.7
SiO_2	<0.01	0.09
Al_2O_3	0.05	0.2
TiO_2	<0.01	0.08
Fe_2O_3	<0.01	0.01
CaO	<0.01	0.01
HfO_2	1.89	1.84
ZrO_2	Bal.	Bal.

2.3 Porosity and Microstructure

2.3.1 Scanning Electron Microscopy. JEOL 6340F FEG-SEM was used to study the coating microstructure. As-sprayed coatings exhibit the characteristic layered structure of PS coatings. The structure within the splat shows columnar grains (Fig. 2). Microcracks and intersplat porosity, as shown in Fig. 1, mostly have slit type geometry. Heat-treatment results in grain growth, often bridging interfaces between splats in close physical proximity, as shown in Fig. 2. There is also evidence of the healing of microcracks and formation of sintering necks. However, large voids remain relatively unaffected.

2.3.2 Mercury Intrusion Porosimetry. A MicroMeritics AutoPore IV (one micromeretics drive, Norcross, GA 30093-1877) was used to estimate the pore size distribution and the total volume of surface-connected porosity. Known mass of the sample was placed in a glass penetrometer, which was evacuated and then back-filled with mercury. Since mercury behaves as a non-wetting liquid for most oxide systems, it needs to be forced into the specimen by application of external pressure. The pressure required being inversely proportional to the pore width, in accordance with the Washburn equation (Ref 20) for slit-like pores:

$$P = -\frac{2\gamma\cos\theta}{w}, \quad \text{(Eq 3)}$$

where P is the applied pressure, γ is the surface tension of mercury (taken as 0.485 N m^{-1}), θ is the contact angle (taken as 130°), and w is the slit width. The penetrometer was progressively pressurized up to ~200 MPa, with the penetration volume being monitored by measuring the capacitance of a co-axial capacitor formed by the intruding mercury and the conducting stem. Pore size distribution was thus obtained, as well as the pore volume.

2.3.3 Gas Adsorption. A MicroMeritics TriStar 3000 (one micromeretics drive, Norcross, GA 30093-1877) was used to measure the specific surface area of detached top coats. Samples were dried thoroughly (~250 °C overnight) in nitrogen before measurement. The sample chambers were then cooled to liquid N_2 temperature and evacuated. Nitrogen was then introduced in controlled pressure increments, and the equilibrated pressures measured and compared with the saturation pressure, to determine the quantities of adsorbed gas. The Brunauer-Emmett-Teller (BET) adsorption isotherm was then used to determine the specimen surface area.

3. Porosity and Pore Architecture

3.1 Specific Surface Area

The surface area of the coatings reduced drastically from ~0.3 $m^2 g^{-1}$ for as-sprayed coatings to ~0.1 $m^2 g^{-1}$ after heat treatment at 1400 °C for 1 h. This reduced further to ~0.08 $m^2 g^{-1}$ when the AB1 samples were heat treated for 10 h. The reduction in surface area is more pronounced for samples with high silica and alumina content (AB2). These samples show >80% reduction in surface area after similar heat treatment. However, at 1200 °C, heat treatment for 20 h caused the surface area of AB1 to reduce to ~0.09 $m^2 g^{-1}$. This drastic reduction in surface area is consistent with the disappearance of small-scale porosity by sintering after heat treatment, observed with mercury intrusion porosimetry (MIP) (Fig. 4). These small pores do not contribute much to the overall porosity, but contribute significantly to the overall surface area (due to high surface-to-volume ratios).

3.2 Porosity and Pore Size Distribution

The pore size distribution obtained from MIP is shown in Fig. 4. It can be seen that the pore size distribution is sensitive to the conditions to which the coatings are subjected prior to testing. While the porosity remained relatively unaffected at ~10-12% even after heat treatment, the pore size distribution changed, indicating reduction in fine scale porosity and redistribution of material, often causing growth of relatively larger pores. The disappearance of fine scale porosity due to sintering would affect various properties of the coating, particularly stiffness.

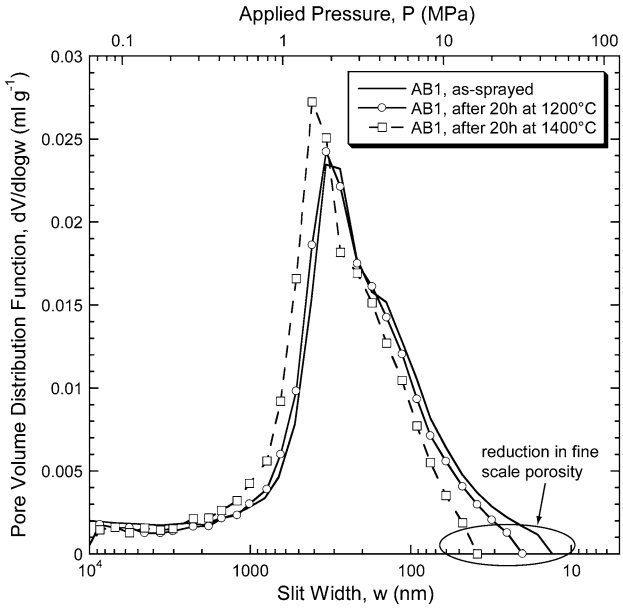

Fig. 4 Mercury intrusion porosimetry data, showing the pore size distributions exhibited by YSZ coatings before and after heat treatment at 1200 and 1400 °C

The pore size distribution was obtained assuming slit-like pore geometry. While this assumption does not affect the deduced pore volume or overall porosity, it would affect the pore size distribution (Ref 21). Another concern regarding analysis of mercury porosimetry data is the presence of "ink-bottle" or "hour-glass" shaped pores (Ref 22). Whenever pores increase in size, beyond a constriction, called the throat, the deduced distribution will be skewed toward finer pores. However, it has been demonstrated that this is not a great problem for widely interconnected network of pores (Ref 23).

Finally, from the deduced pore size distribution and assuming reversible work of intrusion (Ref 24), the specific surface area can be obtained from MIP data using Eq 4:

$$S = -\frac{1}{\gamma \cos\theta} \int_0^V P dV, \qquad \text{(Eq 4)}$$

where S is the specific surface area and V is the volume of mercury intruded at highest applied pressure. Applying this equation, a value $S \sim 0.26$ $m^2 g^{-1}$ was obtained for as-sprayed sample. The value of S reduces to ~0.16 $m^2 g^{-1}$ and ~0.11 $m^2 g^{-1}$ for samples heat treated at 1400 °C for 1 and 10 h, respectively. These values of S are slightly larger than that obtained from BET measurements. Such discrepancies are common (Ref 25), and are often due, at least in part, to the ink-bottle type pores, which skew the distribution toward finer pores, raising the surface area. Another factor that might also contribute to the discrepancy is that the deduction of surface area in Eq 4 is based on the assumption that movement of mercury meniscus in the sample is reversible. As this is rarely the case for interconnected pore network, Eq 4 is not strictly valid for porous samples which contain such interconnected pores. This, however, does not affect the outcome of the above observation, i.e., in the as-sprayed state most of the coating porosity is surface connected.

4. Effect of Pore Architecture on Coating Properties

4.1 Shrinkage

Dilatometry data, where the linear contraction is plotted against time at temperature are presented in Fig. 5. Shrinkage occurs due to sintering of the fine scale features in the top coat. It can also be seen that shrinkage is anisotropic, being greater in the through-thickness direction. This is consistent with the fact that, while intersplat voids and intrasplat microcrack openings are broadly similar in magnitude (~10-300 nm), typical spacing between them are different (~1-4 μm, i.e., the splat thickness, for the voids, compared with ~5-10 μm for the spacing between microcracks). Closure of the voids thus tends to generate greater (through-thickness) shrinkage than similar degrees of closure of microcracks, which

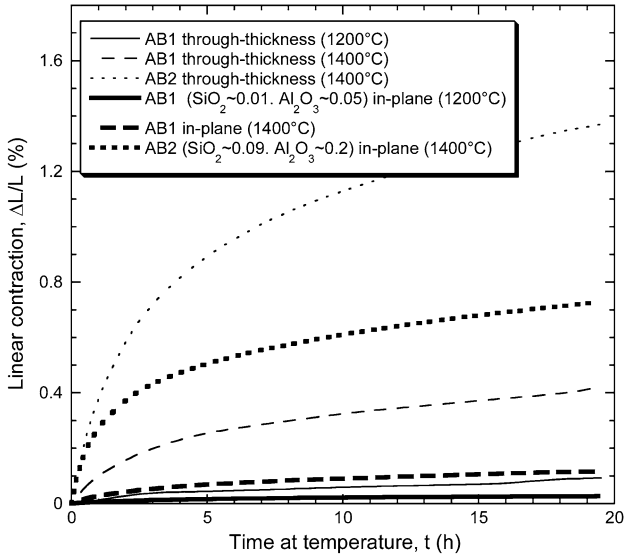

Fig. 5 Dilatometry plots, showing shrinkage exhibited by detached YSZ top coats with different impurity levels during isothermal heat treatment at different temperatures

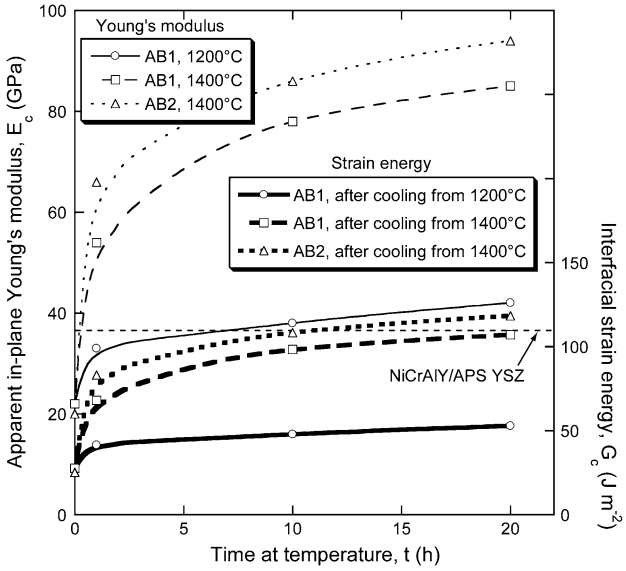

Fig. 6 Apparent in-plane Young's modulus data of detached YSZ top coats subjected to prior heat treatments. The effect of such change in modulus on the interfacial strain energy (i.e., the driving force for debonding) of a 200-μm thick coating on NiCrAlY when cooled by 1000 degrees Celsius is also shown. The *dotted line* represents the reported interfacial fracture energy of a NiCrAlY bond coat/APS top coat interface (Ref 28)

causes in-plane shrinkage. For a given direction, the shrinkage is faster at 1400 °C, and in all cases the rate of contraction falls off with time. It is also clear that higher levels of silica and alumina tend to cause enhanced rates of shrinkage. The dimensional changes corresponding to the dilatometry plot suggest volume shrinkages $\{2(\Delta L/L)_{\text{in-plane}} + (\Delta L/L)_{\text{through-thickness}}\}$ of ~0.7% for AB1 and ~3% for AB2 samples, after heat treatment 1400 °C for 20 h.

The shrinkage suggests that densifying sintering mechanisms are significant at 1400 °C, since, if surface diffusion only were occurring, then it would be expected that the surface area reduction would take place without any shrinkage. However, at lower temperatures surface diffusion mechanisms are likely to dominate.

As the diffusion mechanism (and thus the rate of sintering) is sensitive to the atomic species present, it seems likely that different sintering mechanisms are operative for coatings with high silica and alumina content. It should perhaps be pointed out that liquid-phase sintering may be contributing to the observed effects, particularly with the higher impurity levels and at higher temperatures. Little is known about the formation of vitreous phases in this system, although there are some indications that they can form (Ref 11, 12, 17). However, if substantial quantities were forming during the present experiments, then it would be expected that even the relatively large pores (>100 nm) would start to disappear. In practice, there is no significant change in the volume of such pores (apart from the growth of pores after 20 h at 1400 °C, Fig. 4), which suggests that the vitreous phase content at high temperature is relatively low. Nevertheless, it seems clear that these impurities significantly enhance the diffusion rates, probably for lattice, grain boundary, and surface diffusion.

4.2 Stiffness and Thermal Conductivity

The Young's modulus of as-sprayed top coat was found to be ~22 GPa. This is in good general agreement with the data available in literature taking into account the variation one can have due to different spraying conditions (Ref 13, 14). This value is an order of magnitude lower than the corresponding bulk material. This reduction is attributed to the presence of defects, particularly the fine scale porosity mostly in the form of microcracks. Poor bonding between splats can also lead to sliding of the splats past each other, thus leading to a low macroscopic stiffness. These defects results in high compliance of the as-sprayed coating, allowing it to accommodate thermal and mechanical strains induced during service.

While in service, the stiffness of the top coat changes and this has been presented in Fig. 6. It can be seen that substantial increase in stiffness can arise due to sintering, particularly after heat treatment at 1400 °C and for coatings with more impurities (AB2). The stiffness plots show an initial sharp rise followed by a more progressive rise. This general trend has been reported previously (Ref 26). MIP studies of both as-sprayed and heat-treated top coats show that there is a considerable decrease in the volume of fine scale porosity. The pores <~50 nm seem to almost disappear after heat treatment at 1400 °C for 20 h (Fig. 4). This reduction in fine scale porosity, in the form of healing of microcracks is responsible for the sharp increase in the stiffness of these coatings.

Locking of splats as a result of heat treatment also increases the intersplat contact area, raising the through-thickness thermal conductivity of the coating.

As expected, the increase in thermal conductivity is more pronounced when the samples are heat treated at higher temperature (i.e., 1400 °C) and for longer times (Fig. 7). This observation is consistent with both the dilatometry data (Fig. 5) and the stiffness trends (Fig. 6). It is interesting to note that, although stiffness is sensitive to both healing of intersplat voids and intrasplat microcracks, through-thickness thermal conductivity is probably more sensitive to the locking together of the splats, which causes an increase in the intersplat contact area (bridge area). It is evident from MIP that, at 1200 °C, only very fine porosity, distributed in intersplat voids and intrasplat microcracks, is removed (Fig. 4). Better intersplat contact causes an increase in thermal conductivity and reduces the likelihood of splat shearing as a strain-accommodating mechanism, thereby causing a sharp increase in stiffness. When the samples are heat treated at 1400 °C, significant reduction in the sub-100 nm porosity takes place (greater than that observed at 1200 °C), as observed in MIP (Fig. 4). Thus, healing of more intrasplat microcracks and intersplat voids at 1400 °C would bring about greater increases in both thermal conductivity and stiffness, as compared to that at 1200 °C. However, once the fine scale crack-like pores have healed during the early stages of heat treatment, the rate of shrinkage fall, and so does the rate of stiffening and the increase of thermal conductivity.

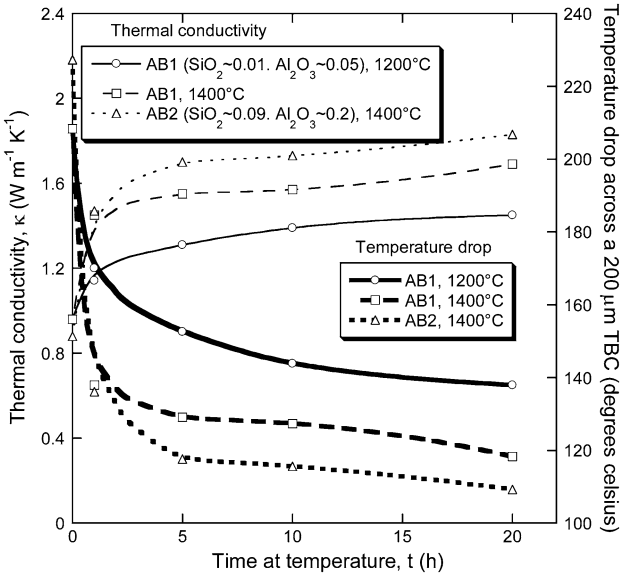

Fig. 7 Through-thickness thermal conductivity of YSZ coatings, before and after thermal treatments, showing the effects of impurity levels and heat-treatment temperature. Consequence of increased thermal conductivity is also shown as reduced thermal protection of the substrate in the form of temperature drop across a 200-μm coating. A constant heat flux ~10 MW m^{-2} was assumed

5. Consequences of Measured Properties

5.1 Consequences of Measured Stiffness

One consequence of the low stiffness in the as-sprayed state is that the heating- and cooling-induced stress, while attached to the substrate, will tend to remain low. Taking the average thermal expansion co-efficient of YSZ top coat as 11×10^{-6} K^{-1}, and that of NiCoCrAlY as $\sim 14 \times 10^{-6}$ K^{-1}, cooling by 1000 °C might typically generate a misfit strain of $\sim 3 \times 10^{-3}$. If this strain were accommodated entirely within a dense zirconia top coat with a Young's modulus of ~200 GPa, the resulting maximum in-plane stress would be ~600 MPa, which would in turn generate a large driving force for debonding of ~250 J m^{-2} for a 200-μm thick coating. This is much higher than the reported bond coat/top coat fracture energies (Ref 27, 28). However, the modulus of the top coat is found to be an order of magnitude lower and consequently, the in-plane stresses and the driving force for debonding are also an order of magnitude lower, so that the coating system is expected to be energetically stable against interfacial debonding during typical temperature changes under service conditions.

However, it is clear from the present work that top coat sintering under service condition can raise its stiffness, and hence the driving force for debonding. If the driving force for debonding exceeds the interfacial fracture energy, then debonding is energetically favored. Tsui (Ref 27) found the critical strain energy release rate for a VPS NiCrAlY bond coat/APS YSZ top coat interface to be ~110 J m^{-2}. However, values as low as ~38 J m^{-2} have also been reported for some bond coat/top coat system (Ref 28). Thus, it appears that stiffening of the top coat is likely to raise the danger of debonding. This danger is probably more pronounced for coatings with higher silica and alumina content (Fig. 6). However, it has been pointed out (Ref 26) that the constraint imposed by attachment to a metallic substrate tends to impose tensile strain on the coating during service and hence inhibit the healing of intrasplat microcracks. This would in turn reduce the stiffness of the top coat in service and hence the driving force for its debonding.* Unfortunately, it is very difficult to carry out isothermal sintering experiments on attached coatings, since the substrates tend to be close to or above their melting temperatures.

5.2 Consequences of Measured Thermal Conductivity

A low thermal conductivity of the top coat is clearly desirable, in terms of improving the performance of gas turbines. For example, the same insulating effect can be achieved with thinner coatings, reducing the parasitic weight, which is particularly desirable for highly loaded components like the turbine blades.

Taking the average temperature drop (ΔT_c) across a 200 μm thick YSZ top coat (with $\kappa \sim 1$ Wm^{-1} K^{-1}) to be

*It is worth noting that these data are all for detached coatings, and it is known that sintering effects are retarded by the tensile strains present when coatings are attached to substrates. However, it probably does not affect the observed trends.

~200 °C, a heat flux (q) of ~10^6 W m^{-2} can be estimated (by using Eq 5).

$$q = -\kappa \frac{\Delta T_c}{\Delta x} \quad \text{(Eq 5)}$$

During operation at elevated temperature, the value of thermal conductivity rises due to sintering, as shown in Fig. 7. A 70% increase in thermal conductivity has been observed after 10 h treatment at 1400 °C (for high purity sample AB1), implying an increase in the back surface temperature by ~80 °C (for the same heat flux). This effect (see footnote) is likely to be further exacerbated by the presence of impurities.

6. Summary and Conclusion

Porosity and pore architecture govern some of the most important thermophysical properties of PS coatings. The presence of large number of defects, in the form of interlamellar pores and microcracks, are responsible for low as-sprayed macroscopic Young's modulus (~22 GPa) and thermal conductivity (~1 W m^{-1} K^{-1}) of the top coats. Sintering causes significant change in the pore architecture after heat treatment, with healing of intra-splat microcracks and enhanced intersplat bonding, which leads to a sharp rise in in-plane stiffness and through-thickness thermal conductivity of the coating. Increase in the contents of alumina and silica by ~10 times (from ~0.01 to ~0.1 wt.%) effects a significant increase in sintering rates, as observed by dilatometry, porosimetry, surface area measurement, stiffness, and thermal conductivity. The increase in Young's modulus of the coatings (particularly with impurities) during service raises questions regarding their reliability as such increase could lead to catastrophic debonding. The protective function of the top coat is also compromised due to increase in its through-thickness thermal conductivity. As sintering effects in TBCs are exacerbated in the presence of impurities such as alumina and silica, the reliability issues mentioned herein should be considered prior to their use.

Acknowledgments

The author highly appreciates the discussions with, and guidance from Professors T. W. Clyne (Cambridge) and H. E. Evans (Birmingham). The author also acknowledges the support from Drs. I.O. Golosnoy (Southampton), R.V. Kumar (Cambridge), A. Cipitria (San Sebastián), and Ms. N. Ibarra-González (Cambridge).

References

1. N.P. Padture, M. Gell, and E.H. Jordan, Thermal Barrier Coatings for Gas-Turbine Engine Applications, *Science*, 2002, **296**, p 280-284
2. R.A. Miller, Current Status of Thermal Barrier Coatings—An Overview, *Surf. Coat. Technol.*, 1987, **30**(1), p 1-11
3. R. Vassen, X.Q. Cao, F. Tietz, D. Basu, and D. Stover, Zirconates as New Materials for Thermal Barrier Coatings, *J. Am. Ceram. Soc.*, 2000, **83**(8), p 2023-2028
4. M. van Roode, Ceramic Gas Turbine Development: Need for a 10 year Plan, *J. Eng. Gas Turb. Power*, 2010, **132**(1), p 1-8
5. S. Kuroda and T.W. Clyne, The Quenching Stress in Thermally Sprayed Coatings, *Thin Solid Films*, 1991, **200**, p 49-66
6. M. Ahrens, S. Lampenscherf, R. Vassen, and D. Stover, Sintering and Creep Processes in Plasma-Sprayed Thermal barrier Coatings, *J. Therm. Spray. Technol.*, 2004, **13**(3), p 432-442
7. J. Ilavsky, G.G. Long, A.J. Allen, C.C. Berndt, and H. Herman, Changes in the Microstructure of Plasma-Sprayed Yttria-Stabilized Zirconia Deposits during Simulated Operating Conditions, *Thermal Spray: A United Forum for Scientific and Technological Advances*, C.C. Berndt, Ed., 15-18 Sep 1997 (Indianapolis, IN), ASM International, 1998, p 697-702
8. A.J. Allen, J. Ilavsky, G.G. Long, J.S. Wallace, C.C. Berndt, and H. Herman, Microstructural Characterisation of Yttria-Stabilized Zirconia Plasma-Sprayed Deposits using Multiple Small-Angle Neutron Scattering, *Acta Mater.*, 2001, **49**, p 1661-1675
9. H.E. Evans and R.C. Lobb, Conditions for the Initiation of Oxide-Scale Cracking and Spallation, *Corros. Sci.*, 1984, **24**(3), p 209-222
10. S.R. Choi, D. Zhu, and R.A. Miller, Effect of Sintering on Mechanical Properties of Plasma-Sprayed Zirconia-Based Thermal Barrier Coatings, *J. Am. Ceram. Soc.*, 2005, **88**(10), p 2859-2867
11. R. Vassen, N. Czech, W. Mallener, W. Stamm, and D. Stover, Influence of Impurity Content and Porosity of Plasma-Sprayed Yttria-Stabilized Zirconia Layers on the Sintering Behaviour, *Surf. Coat. Technol.*, 2001, **141**(2-3), p 135-140
12. S. Paul, A. Cipitria, I.O. Golosnoy, L. Xie, M.R. Dorfman, and T.W. CLyne, Effects of Impurity Content on the Sintering Characteristics of Plasma-Sprayed Zirconia, *J. Therm. Spray. Technol.*, 2007, **16**(5-6), p 798-803
13. D. Schwingel, R. Taylor, T. Haubold, J. Wirgenn, and C. Gaulco, Mechanical and Thermophysical Properties of Thick PYSZ Thermal Barrier Coatings: Correlation with Microstructure and Spraying Parameters, *Surf. Coat. Technol.*, 1998, **108-109**, p 99-106
14. J.S. Wallace and J. Ilavsky, Elastic Modulus Measurements in Plasma Sprayed Deposits, *J. Therm. Spray. Technol.*, 1998, **7**(4), p 521-526
15. R.W. Trice, Y.J. Su, J.R. Mawdsley, K.T. Faber, A.R. De Arellano-Lopez, H. Wang, and W.D. Porter, Effect of Heat Treatment on Phase Stability, Microstructure, and Thermal Conductivity of Plasma-Sprayed YSZ, *J. Mater. Sci.*, 2002, **37**(11), p 2359-2365
16. P. Michlik and C. Berndt, Image-Based Extended Finite Element Modeling of Thermal Barrier Coatings, *Surf. Coat. Technol.*, 2006, **201**(6), p 2369-2380
17. H.C. Chen, E. Pfender, and J. Heberlein, Plasma-Sprayed ZrO_2 Thermal Barrier Coatings Doped with an Appropriate Amount of SiO_2, *Thin Solid Films*, 1998, **315**(1-2), p 159-169
18. S.E. Gustafsson, Transient Plane Source Techniques for Thermal Conductivity and Thermal Diffusivity Measurements of Solid Materials, *Rev. Sci. Inst.*, 1990, **62**(3), p 797-804
19. J.C. Tan, S.A. Tsipas, I.O. Golosnoy, J.A. Curran, S. Paul, and T.W. Clyne, A Steady-State Bi-Substrate Technique for Measurement of the Thermal Conductivity of Ceramic Coatings, *Surf. Coat. Technol.*, 2006, **201**(3-4), p 1414-1420
20. E.W. Washburn, Note on a Method of Determining the Distribution of Pore Sizes in a Porous Materials, *Proc. Natl. Acad. Sci. USA*, 1921, **7**, p 115-116
21. J. Ilavsky, C.C. Berndt, and J. Karthikeyan, Mercury Intrusion Porosimetry of Plasma-Sprayed Ceramic, *J. Mater. Sci.*, 1997, **32**(15), p 3925-3932
22. L. Moscou and S. Lub, Practical Use of Mercury Porosimetry in the Study of Porous Solids, *Powder Technol.*, 1981, **29**, p 45-52
23. N.C. Wardlaw and M. McKellar, Mercury Porosimetry and the Interpretation of Pore Geometry in Sedimentary-Rocks and Artificial Models, *Powder Technol.*, 1981, **29**(1), p 127-143

24. H.M. Rootare and C.F. Prenzlow, Surface Areas from Mercury Porosimeter Measurements, *J. Phys. Chem.*, 1967, **71**(8), p 2733-2736
25. P.J. Dees and J. Polderman, Mercury Porosimetry in Pharmaceutical Technology, *Powder Technol.*, 1981, **29**, p 187-197
26. J.A. Thompson and T.W. Clyne, The Effect of Heat Treatment on the Stiffness of Zirconia Top Coats in Plasma-Sprayed TBCs, *Acta Mater.*, 2001, **49**(9), p 1565-1575
27. Y.C. Tsui, ''Adhesion of Plasma Sprayed Coatings,'' Ph.D. Thesis, University of Cambridge, 1996
28. Y.C. Tsui and T.W. Clyne, Adhesion of Thermal Barrier Coating Systems and Incorporation of an Oxidation Barrier Layer, *Thermal Spray: Practical Solutions for Engineering Problems*, C.C. Berndt. Ed., 7-11 Oct 1996 (Cincinnati, OH), ASM International, 1996, p 275-284